NANO LETTERS

pubs.acs.org/NanoLett
Letter

Molecular Order Induced Charge Transfer in a C_{60}-Topological Insulator Moiré Heterostructure

Ram Prakash Pandeya,* Konstantin P. Shchukin, Yannic Falke, Gregor Mussler, Abdur Rehman Jalil, Nicolae Atodiresei, Eddwi H. Hasdeo, Alexander Fedorov, Boris V. Senkovskiy, Daniel Jansen, Giovanni Di Santo, Luca Petaccia, and Alexander Grüneis*

Cite This: *Nano Lett.* 2025, 25, 1220−1225

ABSTRACT: We synthesized and spectroscopically investigated monolayer (ML) C_{60} on the topological insulator (TI) Bi_4Te_3. This C_{60}/Bi_4Te_3 heterostructure is characterized by an excellent translational order in a novel (4 × 4) C_{60} superstructure on a (9 × 9) cell of Bi_4Te_3. Angle-resolved photoemission spectroscopy (ARPES) of C_{60}/Bi_4Te_3 reveals that ML C_{60} accepts electrons from the TI at room temperature, but no charge transfer occurs at low temperatures. This temperature-dependent doping is further investigated by Raman spectroscopy, photoluminescence (PL), and calculations of C_{60}/Bi_4Te_3. At low temperatures, Raman spectroscopy and PL show a dramatic intensity increase of the C_{60}-related signal, suggesting a transition to a rotationally ordered state. Calculations explain the charge transfer by C_{60} adsorption to Bi_4Te_3 surface defects. The temperature dependence of the charge transfer is attributed to the orientational order of C_{60}. The electron affinity of C_{60} increases at low temperatures due to the freezing of the rotational motion.

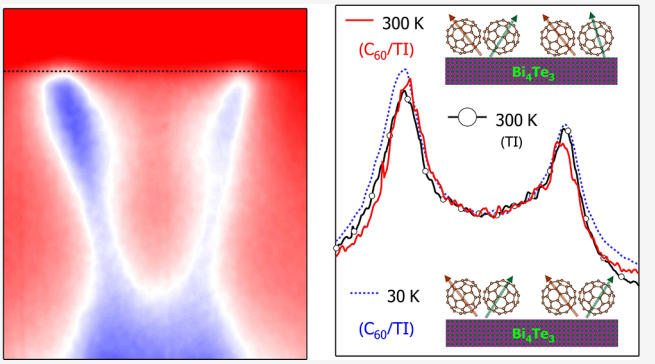

KEYWORDS: *topological insulators, fullerene, angle-resolved photoemission, Raman, photoluminescence*

Organic thin films on metals or semiconductors form interfaces with exciting optoelectronic properties that are controlled by charge transfer and molecular order.[1] Two crucial quantities for obtaining defined interfaces are the relative strengths of the molecule−molecule versus the molecule−substrate interactions.[2] Molecule−substrate interaction imprints molecular order but is detrimental to inheriting the molecular properties from the interface electronic states. The surfaces of bulk metals and semiconductors often strongly bond to molecules, because dangling bonds are present on their surfaces. Their structure is complicated by surface reconstructions, change in molecular shape, and geometrical frustration.[3−5] Van-der-Waals substrates have a relatively weaker interaction with deposited molecules; for example, for pentacene on graphene, a coverage and substrate doping dependent molecular orientation has been observed.[6] For C_{60}/graphene, p-doping[7,8] and a Fermi-level-dependent charge transfer to graphene were observed.[9] Van-der-Waals epitaxy and interaction of organic molecules have been investigated for PTCDA on graphene,[10] C_{60} on hBN,[11,12] C_{60} on WSe_2,[13] borophene on hBN,[14] and PTCDA on borophene.[15] Such heterostructures are useful for transistors and optoelectronic devices.[16−21] The organic layer/topological insulator (TI) system provides a new material system that allows us to study the interaction of the molecules with topologically protected surface electronic states. Molecule−TI interactions have been investigated for monolayers of MnPc,[22] CuPc,[22,23] and CoTBrPP[24] on Bi_2Te_3 and CoPc,[24,25] H_2Pc,[26] and PTCDA[27] on Bi_2Se_3. The electronic structure of highly ordered C_{60} with a thickness of 50 Å on Bi_2Se_3 TI has been investigated, and good agreement with density functional theory (DFT) calculations was found.[28] The large C_{60} thickness prevented the study of the structure of the buried interface. Although single-layer C_{60} on Bi_2Se_3 has been studied, revealing no significant change in substrate band structure, the effect of long-range molecular ordering is yet to be explored.[26] Therefore, the charge transfer between the TI and C_{60}, the effect of C_{60} on the dispersion of the TI surface state, the molecular orientation, and the optical properties of the interface are not known. Moreover, the role of defects of the TI surface in the charge transfer to the organic adsorbate layer has not been investigated.[29,30] Thick films of C_{60} have a structural phase transition from face centered cubic

Received: December 9, 2024
Revised: January 8, 2025
Accepted: January 8, 2025
Published: January 13, 2025

https://doi.org/10.1021/acs.nanolett.4c06294
Nano Lett. 2025, 25, 1220−1225

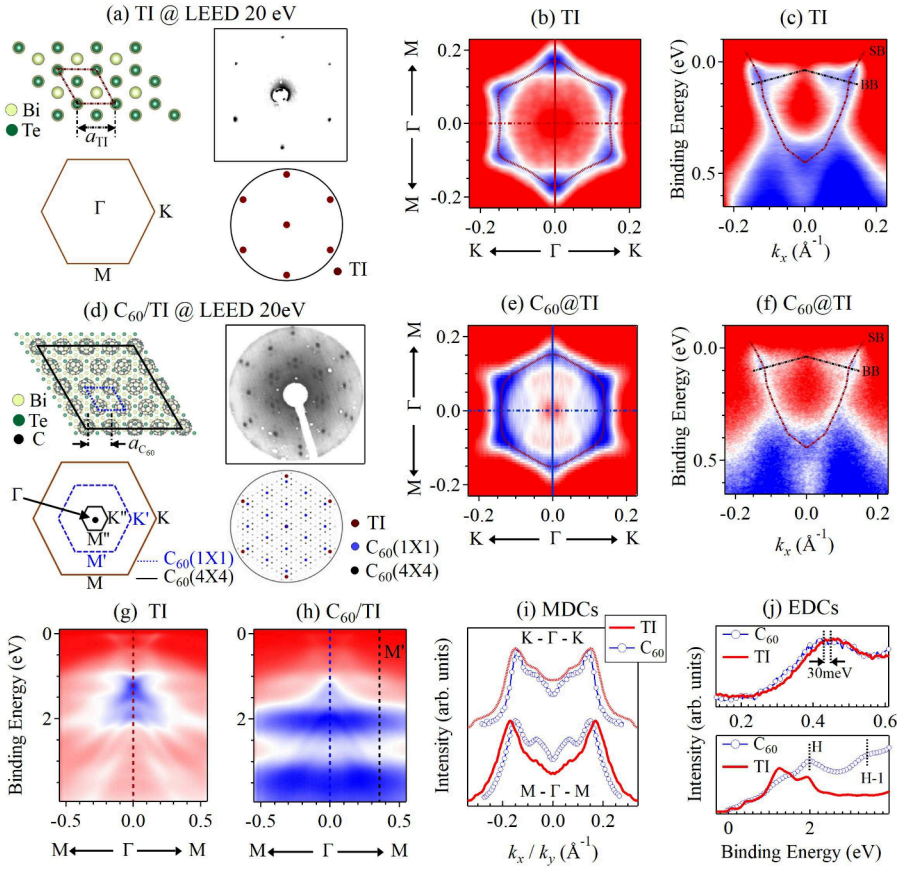

Figure 1. (a) Upper row: surface crystal structure and LEED pattern of Bi_4Te_3. Lower row: Bi_4Te_3 BZ and a sketch of the LEED pattern. (b) Fermi surface of Bi_4Te_3 and tight-binding (TB) fit of the TI surface state (red). (c) ARPES of Bi_4Te_3 along the Γ*K* direction. The surface bands (SB) and bulk bands (BB) are indicated. (d) Upper row: surface unit cell with the 4 × 4 C_{60} superstructure on 9 × 9 TI, the BZ, and a sketch of the surface unit cell. Lower row: LEED pattern of monolayer C_{60} on Bi_4Te_3 and sketch of the LEED pattern reflexes from Bi_4Te_3, C_{60}, and C_{60} superstructure. (e) Fermi surface of C_{60}/Bi_4Te_3 along with a TB fit of the TI surface state (red). (f) ARPES scan of C_{60}/Bi_4Te_3 along the Γ*K*. (g and h) ARPES of Bi_4Te_3 and C_{60}/Bi_4Te_3 in a wide energy range including the HOMO and HOMO−1 of C_{60} at 2 and 3.5 eV, respectively. (i) Momentum dispersion curves (MDCs) at E_F of Bi_4Te_3 and C_{60}/Bi_4Te_3 along Γ*K* and Γ*M*. (j) Energy distribution curves (EDCs) of Bi_4Te_3 and C_{60}/Bi_4Te_3 at Γ in a narrow energy range around the Dirac point and in a wide energy range. The labels H and H−1 indicate the HOMO and HOMO−1 levels. All ARPES data are taken at 300 K with $h\nu$ = 21.2 eV.

(fcc) to simple cubic (sc) at 250 K.[31,32] For fcc (sc), neighboring C_{60} have different (identical) orientation.[32,33] This phase transition affects the Raman and photoluminescence (PL) spectra. Below the transition temperature the Ag(2) (pentagonal pinch) Raman mode hardens and becomes more intense and sharper[31,34] and the PL intensity increases.[35] It is unclear whether that phase transition occurs for a C_{60} monolayer and how it is affected by the substrate.

The low-energy electron diffraction (LEED) pattern of MBE-grown[36] Bi_4Te_3 is shown in Figure 1a along with sketches of the LEED pattern, the (0001) surface of Bi_4Te_3, and the first Brillouin zone (BZ). Figure 1b shows the hexagonally warped, n-type Fermi surface of Bi_4Te_3 measured by angle-resolved photoemission spectroscopy (ARPES) along with a tight-binding (TB) fit to ARPES maxima.[37,38] From the TB fit, we determine the value of the ratio between hexagonal warping λ to Fermi velocity v of λ/v = 27 Å^2. Using the Fermi surface size, we estimate the carrier concentration as $n = 8.98 \times 10^{12}$ cm^{-2}. Figure 1c depicts an ARPES scan through the BZ center along Γ*K* in the vicinity of E_F. The size and shape of the Fermi surface are qualitatively similar to bulk Bi_4Te_3.[38]

Figure 1d depicts the LEED pattern of one ML of C_{60} evaporated on Bi_4Te_3 along with sketches of the LEED pattern and interface as well as the reciprocal lattice of the new supercell. LEED shows the diffraction spots of Bi_4Te_3 and the additional spots that come from C_{60}. From LEED we observe that the reciprocal lattice vector corresponding to the C_{60} lattice is almost half of a Bi_4Te_3 reciprocal lattice vector. Since the lattice constant of the C_{60} layer is not close to an integer multiple of the lattice constant of Bi_4Te_3, a large moiré pattern forms. The set of diffraction spots of weak intensity around each C_{60} diffraction spot are due to that moiré pattern that C_{60} forms on the Bi_4Te_3 surface. In the lower right panel of Figure 1d, the diffraction spots are color-coded according to their origin. The pattern inherits the same orientation as the interface and is due to the arrangement of C_{60} in a (9 × 9) superstructure with respect to the TI lattice, as sketched in the upper left panel of Figure 1d. The new moiré supercell contains 16 C_{60} molecules and is defined by a lattice vector of ∼4 nm in length. The bottom left panel of Figure 1d depicts the BZ of Bi_4Te_3 along with the C_{60} and the moiré BZs. Based on $a_{Bi_4Te_3}$, the lattice constant of Bi_4Te_3, we estimate the C_{60} lattice on Bi_4Te_3 to be (9/4) × $a_{Bi_4Te_3}$ = 10.15 Å. The C_{60} lattice constant in the fcc structure is $a^{fcc}_{C_{60}}$ = 14.12 Å.[39] Hence, the lattice constant of a hexagonal lattice defined on the

https://doi.org/10.1021/acs.nanolett.4c06294
Nano Lett. 2025, 25, 1220−1225

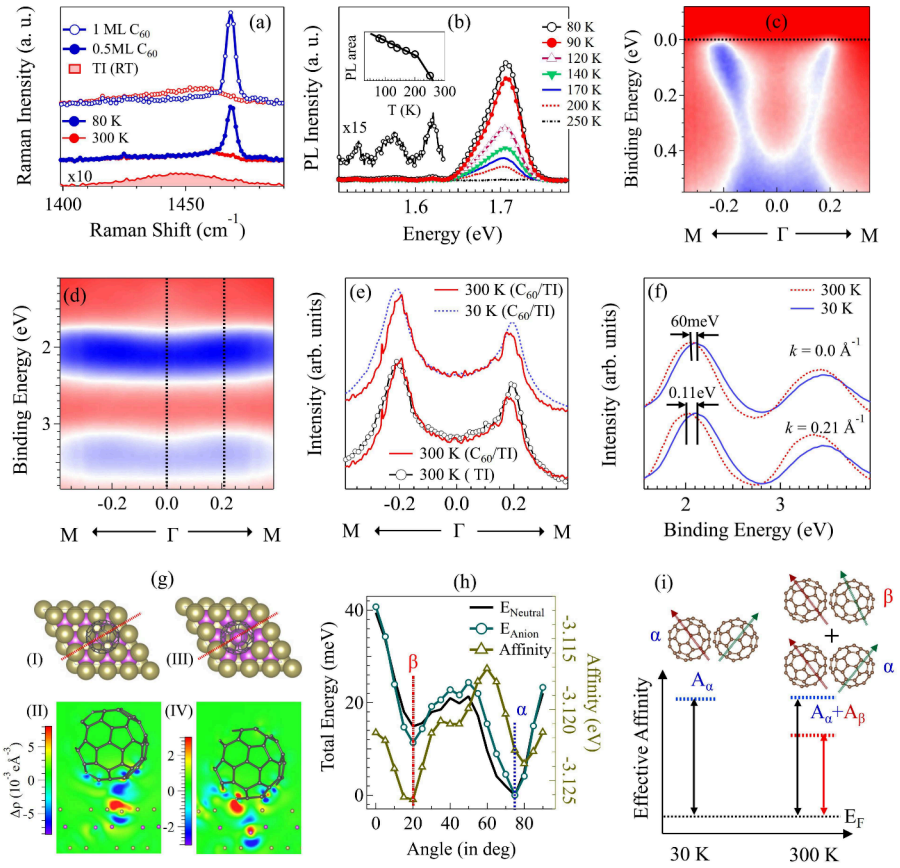

Figure 2. (a) Raman spectra (λ_{exc} = 532 nm) of C_{60}/Bi_4Te_3 at 80 K and at 300 K for 0.5 and 1 ML C_{60} coverages (the C_{60} Ag(2) mode is shown) and the Bi_4Te_3 Raman spectrum for comparison. (b) Temperature-dependent photoluminescence (PL) spectra of C_{60}/Bi_4Te_3 (λ_{exc} = 532 nm). The inset shows the integrated PL intensity. The magnified region shows the phonon side peaks. (c, d) ARPES of C_{60}/Bi_4Te_3 at 30 K in the energy regions of the TI surface state and the HOMO/HOMO−1 states. (e) MDCs at E_F of Bi_4Te_3 at 300 K and C_{60}/Bi_4Te_3 at 300 and 30 K taken along ΓM. (f) EDCs of C_{60}/Bi_4Te_3 through HOMO and HOMO−1 bands at two wavevectors measured at 30 and 300 K. (g) Adsorbed C_{60} onto (I) Te-terminated Bi_4Te_3 and (II) the adsorption induced charge accumulation difference $\Delta\rho$ (red and blue are positive and negative $\Delta\rho$, respectively) along the red line in (I). (III) and (IV) depict the geometry and $\Delta\rho$ for C_{60} on a Te triple vacancy. (h) Total energy of a C_{60} dimer (neutral and anion) (left) and electron affinity (right) vs the rotation angle between the two constituent C_{60}. Angles α and β denote the global and local minima of the total energy. (i) Schematic diagram of dimers with angles α and β between C_{60}. At low temperature, all dimers are in the ground state with the relative rotational angle α. At high temperatures, the state with angle β between C_{60} becomes populated. State β has a lower E_A, explaining why C_{60} is ionized more easily at higher temperature.

fcc(111) plane is $a^{fcc}_{C_{60}}/\sqrt{2}$ = 10.01 Å, implying that the C_{60} monolayer on Bi_4Te_3 is strained by 1.4%.

The Fermi surface of C_{60}/Bi_4Te_3 measured by ARPES is shown in Figure 1e. Performing a TB fit, λ/v = 22 Å^2 and n = 7.59 × 10^{12} cm^{-2} are obtained. Compared to pristine Bi_4Te_3, Bi_4Te_3 with C_{60} on its surface has smaller hexagonal warping and is p-doped. We estimate an average charge transfer of 0.035 hole per C_{60}. Figure 1f shows the ARPES scan of C_{60}/Bi_4Te_3. The ARPES scans of Figures 1g and 1h show the energy band structures in a wide energy range of pristine Bi_4Te_3 and C_{60}/Bi_4Te_3, respectively. The highest occupied molecular orbital (HOMO) and HOMO−1 energy levels from C_{60} appear at binding energies of ∼2 eV and ∼3.2 eV, respectively. Their 2D energy dispersions are also measured by ARPES with linearly polarized light (Supporting Information). In Figure 1i, the momentum distribution curves (MDCs) at the Fermi energy in ΓK and ΓM directions are shown for Bi_4Te_3 and C_{60}/Bi_4Te_3. The Fermi wavevector reduces for C_{60}/Bi_4Te_3 in both directions. This is consistent with the observed reduction of the Fermi surface after C_{60} evaporation. In Figure 1j, we show the energy distribution curves (EDCs) of Bi_4Te_3 and C_{60}/Bi_4Te_3 at the Γ-point and across the HOMO and HOMO−1 levels. The direct comparison of EDCs for Bi_4Te_3 and C_{60}/Bi_4Te_3 shows a shift of the EDC maximum toward the Fermi level as a result of C_{60} deposition.

Figure 2a depicts Raman spectra recorded at 300 and 80 K for one (0.5) ML of C_{60}/Bi_4Te_3 along with the Raman spectra taken on pristine Bi_4Te_3. The Raman intensity of Bi_4Te_3 is negligible compared to the C_{60} Raman intensity. At 300 K, a broad Ag(2) C_{60} Raman mode in the spectrum of C_{60}/Bi_4Te_3 can be detected at around 1450 cm^{-1}. At 80 K, the Ag(2) mode shifts to higher energy and becomes narrower and more intense. The energy upshift, increased Raman intensity, and narrower peak at low temperatures are similar to the fcc to sc transition in μm thick C_{60} films.[31,32,34] At temperatures below the phase transition (250 K), the rotational motion of C_{60} is frozen. In a previous work[34] using a 514 nm laser, the measured Raman intensity of the Ag(2) mode increases by a factor ∼2 when cooled from 280 K to 40 K. Let us now look at the intensity ratio of the 1450 cm^{-1} Raman peaks at 80 K and at 300 K in Figure 2a. Comparing the peak Raman intensity ratios for the 0.5 (1.0) ML curves for 80 and 300 K, we obtain 5.9 (5.5) (±0.5). We believe that the differences of the

https://doi.org/10.1021/acs.nanolett.4c06294
Nano Lett. 2025, 25, 1220−1225

temperature-dependent Raman intensity increase of C_{60}/Bi_4Te_3 and thick C_{60} films can be explained by the dielectric environments, band gaps, resonance conditions, and de-excitation processes.

Figure 2b depicts PL spectra at temperatures between 300 and 80 K. Upon cooling below ∼250 K, the PL intensity at 1.7 eV increases. Matus et al.[35] relate the PL increase of C_{60} films at low temperature to the phase transition from fcc to sc. At temperatures above the phase transition, the rotation of C_{60} causes electron−hole excitation to remain on one C_{60}. Adjacent C_{60} molecules rotate, and there is insufficient overlap between them. Thus, the excitation cannot be transferred and is zero-dimensional. If the temperature is decreased, the fullerenes do not rotate and the overlap between neighboring C_{60} increases. That is, the electronic structure becomes three-dimensional, and an exciton delocalizes over more than one C_{60}. Excitons can diffuse through the crystal until they recombine radiatively at a defect.[35] Additionally, the PL increase at low temperatures could be related to the loss of nonradiative decay channels that require temperature activation and the absence of electron transfer from the Bi_4Te_3 to C_{60}. The PL spectra of C_{60} have side peaks due to coupling to phonons that are red-shifted from the main peak by the phonon energy. We find peaks shifted by 80, 130, and 240 meV from the main PL peak (magnified spectrum in Figure 2b). We compare the peak energies to the phonons of C_{60} and find a reasonable agreement with calculated phonons[40] at 78 meV (H_u^5), 127 meV (T_{3u}^3), and the third overtone of H_u^5 at 234 meV. Note that vibronic and phonon sidebands have also been observed previously in 1 μm thick C_{60} films.[41]

Figures 2c and 2d depict ARPES of C_{60}/Bi_4Te_3 recorded at 30 K in energy ranges of the Dirac cone of Bi_4Te_3 and the molecular C_{60} bands, respectively. Figure 2e shows a comparative MDC analysis of the ARPES spectra of pure Bi_4Te_3 and C_{60}/Bi_4Te_3 at 300 K and C_{60}/Bi_4Te_3 at 30 K carried out on the same sample. MDCs at the Fermi level along the ΓM direction are shown. This Bi_4Te_3 surface was prepared on a different Bi_4Te_3 film than the surface shown in Figure 1, resulting in a slightly different carrier concentration. The analysis in Figure 2e affirms the previous conclusion from Figure 1i; that is, upon C_{60} deposition, the Fermi surface size of Bi_4Te_3 shrinks. From Figure 2e we also observe that, upon cooling C_{60}/Bi_4Te_3 to 30 K, the Fermi surface size increases almost back to the original value of pristine Bi_4Te_3; that is, we have a temperature-dependent charge transfer between C_{60} and Bi_4Te_3. Figure 2f depicts the EDCs of the ARPES data from Figure 2c at 300 K and at 30 K. The two intense peaks correspond to the HOMO and the HOMO−1 of C_{60}. It can be seen that the HOMO and HOMO−1 bands shift to higher binding energy by 60 meV and by 110 meV, respectively, when cooling down the sample from 300 K to 30 K. This downshift is not due to electron doping of C_{60} because also the LUMO (not visible in ARPES) shifts to a higher energy when the sample is cooled. The LUMO upshift follows from DFT calculations. As a consequence of the concurrent downshift of HOMO and upshift of LUMO, C_{60} is p-doped. In order to rationalize the observed findings regarding the charge transfer, we consider two effects. First, we calculate the charge transfer of C_{60} to the unfaulty TI surface and to a realistic TI surface with Te vacancies. Second, we calculate the temperature-dependent change transfer between C_{60} and Bi_4Te_3 by DFT using a C_{60} dimer model with a temperature-dependent rotational angle between the two C_{60}. Figure 2g (subfigures I and II) shows DFT calculations of the geometry and the electron density of an isolated C_{60} adsorbed onto the Te-terminated Bi_4Te_3 surface. C_{60} adsorbs 3.09 Å above the surface with respect to a Te surface atom. The interaction energy of the physisorbed C_{60} onto the TI surface is −0.716 eV. From a Bader charge density analysis of C_{60}/Bi_4Te_3, we identify an electron transfer from C_{60} to Bi_4Te_3 of 0.042 electron, suggesting that the Bi_4Te_3 substrate is slightly n-doped, in contradiction to the ARPES results. In Figure 2g (subfigures III and IV), we consider C_{60} adsorbed to a triple Te vacancy defect on Bi_4Te_3. In this geometry, C_{60} is 1.10 Å above the surface and can directly interact with Bi. As a consequence, the interaction energy of C_{60} on a triple vacancy equals −1.229 eV. Performing a Bader charge density analysis we find that 0.208 electron is transferred from Bi_4Te_3 to one C_{60}, explaining ARPES results at room temperature. Note that for an antisite defect where a Te atom is replaced by a Bi atom[29,30] in the topmost layer, we would also expect electron transfer from Bi_4Te_3 to C_{60} and thus consistency with ARPES observations.

We now consider the effect of the rotational order of adjacent C_{60} on the charge transfer. The electron affinity E_A is defined as the difference in the total energy between the negatively charged system and the neutral system. For the case of strong electron acceptors such as C_{60}, the negatively charged system (with one extra electron in the LUMO) has a lower total energy, which leads to negative values of E_A. The calculations of the realistic C_{60}/Bi_4Te_3 supercell are prohibitively demanding, and we thus consider a $C_{60}-C_{60}$ dimer as a model to qualitatively show the effect of relative rotation. Figure 2h depicts the total energy and E_A of the C_{60} dimer as a function of the C_{60} relative rotation angle. There is one global minimum at a relative rotational angle of ∼75° (α-phase). Another local minimum is located at a relative rotational angle of ∼20° (β-phase). We therefore expect that at low temperatures all C_{60} are in the α-phase, and at room temperature, some of the C_{60} molecules occupy the β-phase due to small energy difference between the two phases. We consider the electron affinity E_A of these two phases in order to explain the observed temperature-dependent charge transfer to Bi_4Te_3 from C_{60}. For the α-phase, the $E_A = -3.123$ eV and for the β-phase, $E_A = -3.126$ eV. The smaller value of E_A for the β-phase means that in this phase the energy gain per C_{60} is larger, if an electronic charge is transferred from Bi_4Te_3. That is, if more C_{60} dimers are in the β-phase, then they can accept more electrons. These calculations qualitatively explain the experimental observation that at 300 K we have a smaller Bi_4Te_3 Fermi surface than at 30 K. The limitations of the calculations are the simplification of using the C_{60} dimer versus the real interface, which ignores the effects of each C_{60} having six nearest C_{60} neighbors and the effect of substrate interaction. Figure 2i depicts E_A for the α- and β-phases of the C_{60} dimer as a function of temperature. At 30 K the α-phase contributes and C_{60} dimers in this phase have a high E_A. As a consequence, it is energetically not favorable to transfer an electron from Bi_4Te_3 to C_{60}. At 300 K, also the β-phase contributes, which lowers the effective E_A, making it energetically favorable to transfer electrons from Bi_4Te_3 to C_{60}.

In conclusion, the moiré structure at the C_{60}/Bi_4Te_3 interface could be observed in ML C_{60} films on Bi_4Te_3 by LEED. The Raman modes and the PL response of C_{60} in the C_{60}/Bi_4Te_3 heterostructure are enhanced at 30 K due to freezing of C_{60} rotation. ARPES of C_{60}/Bi_4Te_3 at 300 K reveals

https://doi.org/10.1021/acs.nanolett.4c06294
Nano Lett. 2025, 25, 1220−1225

an electron transfer from Bi_4Te_3 to C_{60} but no electron transfer at 30 K. Calculations of realistic C_{60} adsorption geometries on triple Te vacancies of Bi_4Te_3 and the temperature-dependent E_A of a C_{60} dimer explain the experimental results. Our work illustrates the complex temperature-dependent interplay between charge transfer and molecular order and is relevant for describing molecule−surface interactions. Future experiments in this direction could use magnetic fullerenes on TI or study the interface between TI and superconducting alkali metal doped fullerene film (e.g., TI/Rb_3C_{60}).

■ ASSOCIATED CONTENT

Supporting Information

The Supporting Information is available free of charge at https://pubs.acs.org/doi/10.1021/acs.nanolett.4c06294.

ARPES characterization of C_{60}/Bi_4Te_3 using polarized synchrotron radiation; experimental and theoretical methods; calculated interaction energies and charge transfer between C_{60} and the defective Bi_4Te_3 surface; analysis of hole doping of Bi_4Te_3 and the charge transfer per C_{60}; evaluation of Te triple vacancy density; dependence of charge transfer on the C_{60}−Bi_4Te_3 distance (PDF)

■ AUTHOR INFORMATION

Corresponding Authors

Ram Prakash Pandeya − *Institut für Festkörperelektronik, Technische Universität Wien, 1040 Vienna, Austria; II. Physikalisches Institut, Universität zu Köln, 50937 Köln, Germany*; Email: ram.pandeya@tuwien.ac.at

Alexander Grüneis − *Institut für Festkörperelektronik, Technische Universität Wien, 1040 Vienna, Austria; II. Physikalisches Institut, Universität zu Köln, 50937 Köln, Germany*; orcid.org/0000-0003-2448-6060; Email: alexander.grueneis@tuwien.ac.at

Authors

Konstantin P. Shchukin − *Institut für Festkörperelektronik, Technische Universität Wien, 1040 Vienna, Austria; II. Physikalisches Institut, Universität zu Köln, 50937 Köln, Germany*

Yannic Falke − *II. Physikalisches Institut, Universität zu Köln, 50937 Köln, Germany*

Gregor Mussler − *Peter Grünberg Institut (PGI-9), Forschungszentrum Jülich, D-52425 Jülich, Germany*

Abdur Rehman Jalil − *Peter Grünberg Institut (PGI-9), Forschungszentrum Jülich, D-52425 Jülich, Germany*; orcid.org/0000-0003-1869-2466

Nicolae Atodiresei − *Peter Grünberg Institut (PGI-1), Forschungszentrum Jülich, D-52425 Jülich, Germany*

Eddwi H. Hasdeo − *Department of Physics and Materials Science, Universite' du Luxembourg, L-1511 Luxembourg, Luxembourg; Research Center for Quantum Physics, National Research and Innovation Agency, 15314 South Tangerang, Indonesia*

Alexander Fedorov − *II. Physikalisches Institut, Universität zu Köln, 50937 Köln, Germany; Leibniz Institute for Solid State and Materials Research, 01069 Dresden, Germany*

Boris V. Senkovskiy − *II. Physikalisches Institut, Universität zu Köln, 50937 Köln, Germany*; orcid.org/0000-0003-1443-6780

Daniel Jansen − *II. Physikalisches Institut, Universität zu Köln, 50937 Köln, Germany*; orcid.org/0009-0002-0763-5853

Giovanni Di Santo − *Elettra Sincrotrone Trieste, 34149 Trieste, Italy*; orcid.org/0000-0001-9394-2563

Luca Petaccia − *Elettra Sincrotrone Trieste, 34149 Trieste, Italy*; orcid.org/0000-0001-8698-1468

Complete contact information is available at: https://pubs.acs.org/10.1021/acs.nanolett.4c06294

Notes

The authors declare no competing financial interest.

■ ACKNOWLEDGMENTS

A.G. and N.A. acknowledge the DFG through CRC 1238 (277146847, A01, and C01). B.S. and A.G. acknowledge DFG projects SE 2575 and INST 216/955-1 FUGG. The stay at the Elettra synchrotron has been supported by the project CALIPSOplus under Grant Agreement 730872 from HORIZON 2020 (EU). We acknowledge Elettra Sincrotrone Trieste for providing access to its synchrotron radiation facilities. N.A. gratefully acknowledges the computing time granted by JARA Vergabegremium and provided on the JARA Partition part of the supercomputer JURECA at Forschungszentrum Jülich. E.H.H. acknowledges financial support from the National Research Fund of Luxembourg under grant C21/MS/15752388/NavSQM and HPC facilities of the University of Luxembourg.[42] We acknowledge discussions with Sasfan Arman Wella and Henry Fried. The authors acknowledge TU Wien Bibliothek for financial support through its Open Access Funding Programme.

■ REFERENCES

(1) Bonifazi, D.; Enger, O.; Diederich, F. Supramolecular fullerene chemistry on surfaces. *Chem. Soc. Rev.* **2007**, *36*, 390−414.

(2) Gruznev, D. V.; Matetskiy, A. V.; Bondarenko, L. V.; Utas, O. A.; Zotov, A. V.; Saranin, A. A.; Chou, J. P.; Wei, C. M.; Lai, M. Y.; Wang, Y. L. Stepwise self-assembly of C60 mediated by atomic scale moiré magnifiers. *Nat. Commun.* **2013**, *4*, 1−7.

(3) Alfonso-Moro, M.; Guisset, V.; David, P.; Canals, B.; Coraux, J.; Rougemaille, N. Geometrical Frustration, Correlated Disorder, and Emerging Order in a Corrugated C_{60} Monolayer. *Phys. Rev. Lett.* **2023**, *131*, 186201.

(4) Pai, W. W.; Jeng, H. T.; Cheng, C.-M.; Lin, C.-H.; Xiao, X.; Zhao, A.; Zhang, X.; Xu, G.; Shi, X. Q.; Van Hove, M. A.; Hsue, C.-S.; Tsuei, K.-D. Optimal Electron Doping of a C_{60} Monolayer on Cu(111) via Interface Reconstruction. *Phys. Rev. Lett.* **2010**, *104*, 036103.

(5) Schull, G.; Berndt, R. Orientationally Ordered (7 × 7) Superstructure of C_{60} on Au(111). *Phys. Rev. Lett.* **2007**, *99*, 226105.

(6) Liu, X.; Grüneis, A.; Haberer, D.; Fedorov, A. V.; Vilkov, O.; Strupinski, W.; Pichler, T. Tunable Interface Properties between Pentacene and Graphene on the SiC Substrate. *J. Phys. Chem. C* **2013**, *117*, 3969−3975.

(7) Qin, S.; Du, Q.; Dong, R.; Yan, X.; Liu, Y.; Wang, W.; Wang, F. Robust, flexible and broadband photodetectors based on van der Waals graphene/C60 heterostructures. *Carbon* **2020**, *167*, 668−674.

(8) Matković, A.; Kratzer, M.; Kaufmann, B.; Vujin, J.; Gajić, R.; Teichert, C. Probing charge transfer between molecular semiconductors and graphene. *Sci. Rep.* **2017**, *7*, 9544.

(9) Nguyen, N. N.; Lee, H. C.; Yoo, M. S.; Lee, E.; Lee, H.; Lee, S. B.; Cho, K. Charge-Transfer-Controlled Growth of Organic Semiconductor Crystals on Graphene. *Adv. Sci.* **2020**, *7*, 1902315.

(10) Wang, Q. H.; Hersam, M. C. Room-temperature molecular-resolution characterization of self-assembled organic monolayers on epitaxial graphene. *Nat. Chem.* **2009**, *1*, 206−211.
(11) Muntwiler, M.; Auwärter, W.; Seitsonen, A. P.; Osterwalder, J.; Greber, T. Rocking-motion-induced charging of C_{60} on *hBN*(111). *Phys. Rev. B* **2005**, *71*, 121402.
(12) Guo, H.; Martínez-Galera, A. J.; Gómez-Rodríguez, J. M. C60 self-orientation on hexagonal boron nitride induced by intermolecular coupling. *Nanotechnology* **2021**, *32*, 025711.
(13) Santos, E. J. G.; Scullion, D.; Chu, X. S.; Li, D. O.; Guisinger, N. P.; Wang, Q. H. Rotational superstructure in van der Waals heterostructure of self-assembled C60 monolayer on the WSe2 surface. *Nanoscale* **2017**, *9*, 13245−13256.
(14) Cuxart, M. G.; Seufert, K.; Chesnyak, V.; Waqas, W. A.; Robert, A.; Bocquet, M.-L.; Duesberg, G. S.; Sachdev, H.; Auwärter, W. Borophenes made easy. *Science Advances* **2021**, *7*, eabk1490.
(15) Liu, X.; Wei, Z.; Balla, I.; Mannix, A. J.; Guisinger, N. P.; Luijten, E.; Hersam, M. C. Self-assembly of electronically abrupt borophene/organic lateral heterostructures. *Science Advances* **2024**, *3*, e1602356.
(16) Huang, X.; Ji, D.; Fuchs, H.; Hu, W.; Li, T. Recent Progress in Organic Phototransistors: Semiconductor Materials, Device Structures and Optoelectronic Applications. *ChemPhotoChem.* **2020**, *4*, 9−38.
(17) Kim, K.; Lee, T. H.; Santos, E. J. G.; Jo, P. S.; Salleo, A.; Nishi, Y.; Bao, Z. Structural and Electrical Investigation of C60-Graphene Vertical Heterostructures. *ACS Nano* **2015**, *9*, 5922−5928.
(18) Oswald, J.; Beretta, D.; Stiefel, M.; Furrer, R.; Lohde, S.; Vuillaume, D.; Calame, M. Field and Thermal Emission Limited Charge Injection in Au-C60-Graphene van der Waals Vertical Heterostructures for Organic Electronics. *ACS Appl. Nano Mater.* **2023**, *6*, 9444−9452.
(19) Kleemann, H.; Krechan, K.; Fischer, A.; Leo, K. A Review of Vertical Organic Transistors. *Adv. Funct. Mater.* **2020**, *30*, 1907113.
(20) Choi, Y. J.; Kim, S.; Woo, H. J.; Song, Y. J.; Hwang, E.; Kang, M. S.; Cho, J. H. Color-Selective Schottky Barrier Modulation for Optoelectric Logic. *ACS Nano* **2020**, *14*, 16036−16045.
(21) He, D.; et al. A van der Waals pn heterojunction with organic/inorganic semiconductors. *Appl. Phys. Lett.* **2015**, *107*, 183103.
(22) Sessi, P.; Bathon, T.; Kokh, K. A.; Tereshchenko, O. E.; Bode, M. Probing the Electronic Properties of Individual MnPc Molecules Coupled to Topological States. *Nano Lett.* **2014**, *14*, 5092−5096.
(23) Bathon, T.; Sessi, P.; Kokh, K. A.; Tereshchenko, O. E.; Bode, M. Systematics of Molecular Self-Assembled Networks at Topological Insulators Surfaces. *Nano Lett.* **2015**, *15*, 2442−2447.
(24) Cuxart, M. G.; Valbuena, M. A.; Robles, R.; Moreno, C.; Bonell, F.; Sauthier, G.; Imaz, I.; Xu, H.; Nistor, C.; Barla, A.; et al. Molecular approach for engineering interfacial interactions in magnetic/topological insulator heterostructures. *ACS Nano* **2020**, *14*, 6285−6294.
(25) Caputo, M.; Panighel, M.; Lisi, S.; Khalil, L.; Santo, G. D.; Papalazarou, E.; Hruban, A.; Konczykowski, M.; Krusin-Elbaum, L.; Aliev, Z. S.; et al. Manipulating the topological interface by molecular adsorbates: adsorption of Co-phthalocyanine on Bi2Se3. *Nano Lett.* **2016**, *16*, 3409−3414.
(26) Jakobs, S.; Narayan, A.; Stadtmueller, B.; Droghetti, A.; Rungger, I.; Hor, Y. S.; Klyatskaya, S.; Jungkenn, D.; Stoeckl, J.; Laux, M.; et al. Controlling the spin texture of topological insulators by rational design of organic molecules. *Nano Lett.* **2015**, *15*, 6022−6029.
(27) Yang, H.-H.; Chu, Y.-H.; Lu, C.-I.; Butler, C. J.; Sankar, R.; Chou, F.-C.; Lin, M.-T. Organic Monolayer Protected Topological Surface State. *Nano Lett.* **2015**, *15*, 6896−6900.
(28) Latzke, D. W.; Ojeda-Aristizabal, C.; Griffin, S. M.; Denlinger, J. D.; Neaton, J. B.; Zettl, A.; Lanzara, A. Observation of highly dispersive bands in pure thin film C_{60}. *Phys. Rev. B* **2019**, *99*, 045425.
(29) Netsou, A.-M.; Muzychenko, D. A.; Dausy, H.; Chen, T.; Song, F.; Schouteden, K.; Van Bael, M. J.; Van Haesendonck, C. Identifying Native Point Defects in the Topological Insulator Bi2Te3. *ACS Nano* **2020**, *14*, 13172−13179.
(30) Dai, J.; West, D.; Wang, X.; Wang, Y.; Kwok, D.; Cheong, S.-W.; Zhang, S. B.; Wu, W. Toward the Intrinsic Limit of the Topological Insulator Bi_2Se_3. *Phys. Rev. Lett.* **2016**, *117*, 106401.
(31) Matus, M.; Kuzmany, H.; Krätschmer, W. Resonance Raman scattering and electronic transitions in C60. *Solid State Commun.* **1991**, *80*, 839−842.
(32) Dresselhaus, M.; Dresselhaus, G.; Eklund, P. *Science of Fullerenes and Carbon Nanotubes*; Academic Press, 1996.
(33) Heiney, P. A.; Fischer, J. E.; McGhie, A. R.; Romanow, W. J.; Denenstein, A. M.; McCauley, J. P., Jr; Smith, A. B.; Cox, D. E. Orientational ordering transition in solid C_{60}. *Phys. Rev. Lett.* **1991**, *66*, 2911.
(34) van Loosdrecht, P. H. M.; van Bentum, P. J. M.; Meijer, G. Rotational ordering transition in single-crystal C_{60} studied by Raman spectroscopy. *Phys. Rev. Lett.* **1992**, *68*, 1176−1179.
(35) Matus, M.; Kuzmany, H.; Sohmen, E. Self-trapped polaron exciton in neutral fullerene C_{60}. *Phys. Rev. Lett.* **1992**, *68*, 2822−2825.
(36) Nabok, D.; Tas, M.; Kusaka, S.; Durgun, E.; Friedrich, C.; Bihlmayer, G.; Blügel, S.; Hirahara, T.; Aguilera, I. Bulk and surface electronic structure of Bi_4Te_3 from *GW* calculations and photoemission experiments. *Phys. Rev. Mater.* **2022**, *6*, 034204.
(37) Fu, L. Hexagonal Warping Effects in the Surface States of the Topological Insulator Bi_2Te_3. *Phys. Rev. Lett.* **2009**, *103*, 266801.
(38) Chagas, T.; Ashour, O. A.; Ribeiro, G. A. S.; Silva, W. S.; Li, Z.; Louie, S. G.; Magalhães-Paniago, R.; Petroff, Y. Multiple strong topological gaps and hexagonal warping in Bi_4Te_3. *Phys. Rev. B* **2022**, *105*, L081409.
(39) Sathish, M.; Miyazawa, K. Synthesis and characterization of fullerene nanowhiskers by liquid-liquid interfacial precipitation: influence of C60 solubility. *Molecules* **2012**, *17*, 3858−3865.
(40) Yu, J.; Kalia, R. K.; Vashishta, P. Phonon dispersion and density of states of solid C60. *Appl. Phys. Lett.* **1993**, *63*, 3152−3154.
(41) Reber, C.; Yee, L.; McKiernan, J.; Zink, J. I.; Williams, R. S.; Tong, W. M.; Ohlberg, D. A. A.; Whetten, R. L.; Diederich, F. Luminescence and absorption spectra of carbon (C60) films. *J. Phys. Chem.* **1991**, *95*, 2127−2129.
(42) Varrette, S.; Bouvry, P.; Cartiaux, H.; Georgatos, F. Management of an academic HPC cluster: The UL experience. *2014 International Conference on High Performance Computing and Simulation (HPCS)*; IEEE: Bologna, Italy, 2014; pp 959−967.

https://doi.org/10.1021/acs.nanolett.4c06294
Nano Lett. 2025, 25, 1220−1225